Cu^+ transient species mediate the reconstruction of copper electrocatalysts for CO_2 reduction

Jan Vavra[a+], Gaétan P. L. Ramona[a+], Federico Dattila[b], Attila Kormányos[c], Tatiana Priamushko[c], Petru P. Albertini[a], Anna Loiudice[a], Serhiy Cherevko[c], Núria Lopéz[b], Raffaella Buonsanti[a*]

[a]Laboratory of Nanochemistry for Energy (LNCE), Institute of Chemical Sciences and Engineering (ISIC), École Polytechnique Fédérale de Lausanne, CH-1950 Sion, Switzerland.

[b]Institute of Chemical Research of Catalonia (ICIQ-CERCA), The Barcelona Institute of Science and Technology (BIST), Tarragona, Spain

[c]Helmholtz-Institute Erlangen-Nürnberg for Renewable Energy (IEK-11), Forschungszentrum Jülich, Cauerstrasse 1, 91058 Erlangen, Germany

*Correspondence to: raffaella.buonsanti@epfl.ch

[+] contributed equally

Abstract

Understanding metal surface reconstruction is of the uttermost importance in heterogeneous catalysis as this phenomenon directly affects the nature of available active sites. However, surface reconstruction is notoriously difficult to study because of the dynamic nature of the phenomena behind it, particularly when solid/liquid interfaces are involved. Here, we report on the intermediates which drive the rearrangement of copper catalysts for the electrochemical CO_2 reduction reaction (CO_2RR). Online mass spectrometry and UV-Vis absorption spectroscopy data are consistent with a dissolution – redeposition process, previously demonstrated by in-situ electron microscopy. The data indicate that the soluble transient species contain copper in +1 oxidation state. Density functional theory identifies copper-adsorbate complexes which can exist in solution under operating conditions. Copper carbonyls

and oxalates are suggested as the major reaction-specific species driving copper reconstruction during CO_2RR. This work motivates future methodological studies to enable the direct detection of these compounds and strategies which specifically target them to improve the catalyst operational stability.

Introduction

A growing interest in sustainable production of chemicals and fuels accompanies the current shift to renewable energy. The electrochemical CO_2 reduction reaction (CO_2RR) is a promising approach to convert waste CO_2 into value added products, such as ethylene or ethanol.[1] Copper is typically used to catalyze the reaction and a great progress has been made in understanding the parameters which govern its activity and selectivity.[1,2] Numerous studies show that the arrangement of Cu surface atoms has profound effect on performance.[3–5] Yet, evidence piles up for the dynamic nature of Cu surfaces under CO_2RR conditions, despite metallic Cu being supposedly stable at the cathodic potentials of CO_2RR.[6–23] Fundamental understanding of these dynamic processes is essential for the technological implementation of CO_2RR, which must target high selectivity and long-term stability both at the catalyst and at the device level.

Various experimental proofs suggest that Cu catalysts reconstruct both during start/stop operation and under the continuously applied cathodic potential during CO_2RR.[6,10–16,18–22] A few studies indicate that Cu electrocatalysts are structurally stable over extended time once fast initial morphological/structural changes are completed.[18–21] Other examples show that these changes continue over the course of CO_2RR.[6,10–16,22] The reconstruction kinetics of Cu electrodes, which differ in surface structure and morphology, might vary. Yet, the mechanism driving their reconstruction is likely to be similar. This mechanism remains mostly unknown.

Copper dissolves transiently during the formation of surface oxides and during the oxide reduction to metallic copper.[15,18–20,23] Thus, these redox processes play a role in the Cu catalyst reconstruction.[15,20,23] These events occur at potentials close to the open circuit potential (OCP) of a typical CO_2RR experiment, which is around +0.4 V_{RHE} (RHE = Reversible Hydrogen Electrode).[15,18] The catalyst typically encounters OCP during the cell assembly and electrolyte introduction and during a start/stop operation. During the cell startup, where the working electrode experiences cathodic potentials, the redeposition of the Cu species dissolved in

solution occurs and induces changes in the catalyst morphology and total exposed surface.[15,20,23]

Under typical potentials for CO_2RR, which are more negative than –0.8 V_{RHE}, the Pourbaix diagram indicates that Cu exists in its metallic state across the entire pH window.[24] Surface science studies have shown that the CO adsorption on Cu can induce metal-metal bond breaking and cluster formation, thus enabling surface reconstruction.[25,26,27] The Cu-CO interactions have been used also in the context of CO_2RR to explain Cu surface reconstruction captured with different in-situ methods.[19, 28] A recent study, based on in-situ electron microscopy, has indicated that a dissolution – redeposition mechanism is responsible for the structural evolution of Cu nanocatalysts.[15] In the case of Cu nanocatalysts, the presence of dissolved Cu species mediates the proposed reconstruction process. However, the chemical nature of these species remains unknown.

Herein, we study the soluble intermediates which drive the reconstruction of copper via complexation with an organic ligand which prolongs the lifetime of the intermediates, allowing their detection. We demonstrate that these transient species contain copper in the +1 oxidation state. Density Functional Theory (DFT) suggests the chemical nature of these species, which are copper carbonyl and copper oxalate complexes as most likely candidates. These molecules are initially adsorbed on the Cu surface as intermediates of the CO_2RR and then enable transient dissolution of Cu by forming coordination complexes with Cu^+ ions.

Results

Catalyst characterization

To investigate the transient species mediating the reconstruction of Cu catalysts during CO_2RR, we chose ~ 7 nm Cu spheres as a model system (Fig. 1A). These small nanoparticles (NPs) expose a large surface area to the electrolyte and possess a relatively high number of undercoordinated atoms on their high-curvature surface. These features account for rapid and irreversible structural transformations in the initial phases of CO_2RR.[7,9,12,29,30] Such short timescales ease the study of the phenomena related to their reconstruction. Furthermore, the low size polydispersity of these Cu NPs is beneficial to form 2D self-assembled monolayers on the surface of the glassy carbon supporting electrode (Fig. 1B), which was utilized to

repeatedly create consistent films with an optimized dip-coating protocol (see Experimental Section for details). Indeed, the measured electrochemically active surface area (ECSA) of the electrodes was reproducible to within 10% (Supplementary Fig. S1.1). The as-synthesized NPs consist of mostly metallic Cu, as evidenced by electron diffraction (Fig. 1C). Here, the observed reflections match with Cu fcc structure. A minor contribution of Cu_2O to the diffraction signal is observed, most visible as a shoulder at 4 nm^{-1} corresponding to Cu_2O {111} reflection.

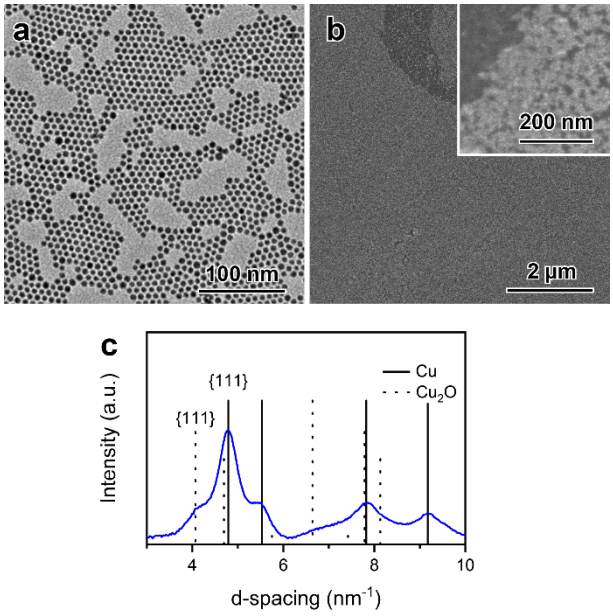

Fig. 1: Characterization of the as-synthesized Cu catalyst. (a) TEM image of the as-synthesized Cu spheres with mean size of around 7 nm; (b) Scanning electron microscopy (SEM) of the Cu spheres deposited on a glassy carbon electrode via dip-coating. The inset shows the (sub)monolayer catalyst packing. (c) Electron diffraction of the as-synthesized catalyst evidencing the metallic nature of the sample. Reflections are assigned to the Cu fcc structure.

The Cu NPs undergo severe reconstruction during the first minutes of CO_2RR; recent studies provided details on the product evolution, the changes of oxidation state, and the structural modifications.[7,9,12,15,29,30] In particular, in-situ electron diffraction and operando X-Ray absorption spectroscopy demonstrated that these same Cu NPs are oxidized at OCP and are in their fully reduced state at the cathodic potentials of CO_2RR.[15] Characteristic Cu_2O cubes were detected by post-mortem analysis (Supplementary Fig. S1.2). This observation is consistent

with literature reports, where the active catalytic phase was shown to be polycrystalline Cu aggregates, while Cu_2O cubes form only ex-situ upon exposure of the sample to air.[9,29,30] *In-situ* liquid-phase TEM has suggested that this reconstruction occurs via a dissolution – redeposition mechanism mediated by dissolved Cu species.[15]

Dissolved Cu detected with on-line ICP-MS

A scanning electrochemical flow cell coupled to an inductively coupled plasma mass spectrometer (on-line ICP-MS) was used to detect the amount of the dissolved species. This system is extremely sensitive and capable of detecting pg cm^{-2} amounts of dissolved Cu ions.[31,32] The dissolution rate of copper is reported as a function of time with the applied current and measured potential (Fig. 2). The cell was operated in chronopotentiometric mode (CP). A low negative baseline current (–0.28 mA cm^{-2}) was applied to the working electrode during the immersion in the electrolyte. This protocol minimizes the catalyst exposure to OCP and focuses the investigation on the operation under cathodic bias (Supplementary Note S.2.1 and Fig. S2.1). Pulses at progressively more negative currents (from –0.55 mA cm^{-2} to –2.95 mA cm^{-2}) were applied for a gradually more extended time (between 20 – 55 s) to simulate the CO_2RR conditions (Fig. 2a). Concomitantly, a progressively more negative potential was measured (Fig.2b). The reported CP profile is a result of parameter optimization (details in the Supplementary Note S2.1). No dependence of the Cu dissolution with the pulse length was observed; however, the longer holds during the more cathodic pulses permitted a more accurate signal integration by enabling the return of both current and potential to the baseline after each pulse.

In the immersion step, a reductive current is applied, which initiates the reduction of copper oxide film on the surface of the electrodes to metallic Cu and induces the transient cathodic dissolution of Cu. Thus, a contact dissolution feature is observed (Fig. 2c, blue curve).[33] No dissolution is detected after that until the last pulse, where the potential reaches –1.1 V_{RHE} (Fig. 2b, blue curve). Following this pulse, a small dissolution signal, close to the detection limit, emerges at 1200s (Fig. 2c, blue curve). Overall, ICP-MS does not detect much Cu in solution. This observation suggests that the redeposition of the soluble Cu species responsible for Cu catalyst reconstruction occurs at a rate that is faster, or at least comparable, to the generation rate, under the investigated regimes. Therefore, the intermediate species must be confined to the vicinity of the working electrode.

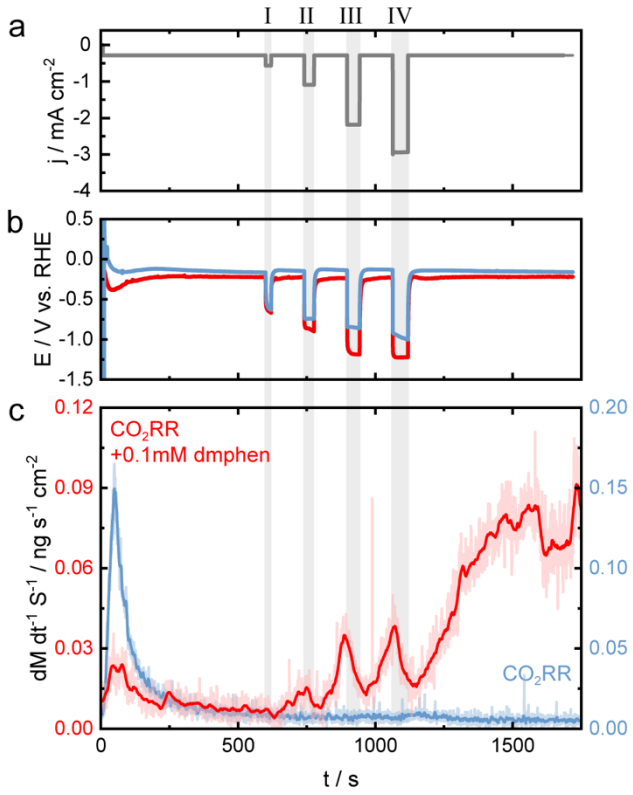

Fig. 2: On-line ICP-MS measuring the dissolution rate of Cu NPs under cathodic bias. (a) Optimized protocol for the applied current: contact with the electrolyte was established while applying –0.28 mA cm^{-2}; after a 600s hold at this current density, four current pulses separated by 120s with gradually increasing cathodic current densities were applied: pulse I (–0.55 mA cm^{-2} for 20 s), pulse II (–1.10 mA cm^{-2} for 35s), pulse III (–2.20 mA cm^{-2} for 45s) and pulse IV (–2.95 mA cm^{-2} for 55 s). (b) Measured cell potential. Data acquired without and with the dmphen are reported in blue and red, respectively. It is noted that the measured potentials in the presence of dmphen are more negative, perhaps for increased solution resistance. (c) Cu mass dissolution rate. 0.05 M $KHCO_3$ saturated with CO_2 was used as the electrolyte. Dmphen was added to the electrolyte (0.1 mM) to prolong the lifetime of the Cu intermediate species. It is noted that all the measured signals do not change suddenly as the potential is applied or removed, at the start and the end of each pulse; instead, they present a tail that is intrinsic to measurements in the flow system. Dissolution curves were denoised using an FFT filter. For the sake of clarity, the original data are presented behind the smoothed curves (pale blue and red curves).

Phenanthrolines are known to strongly coordinate Cu ions.[34–38] Thus, we thought about adding these molecules in the electrolyte to prolong the lifetime of the reconstruction intermediates and enable their reliable detection. Particularly, 2,9-dimethyl-phenanthroline (dmphen) meets the two basic requirements for this study, which are the solubility in water and stability under CO_2RR conditions (details in the Supplementary Note S3.1).

The presence of the dmphen in the electrolyte greatly amplifies the Cu dissolution signal during the pulsed operation, rendering it clearly distinguishable above the baseline (Fig 2c, red curve). Meanwhile, the contact dissolution feature is reduced because a more negative potential needed in the presence of the dmphen. During the current pulses, the dissolution profile changes appreciably. The signal decreases for the duration of the negative current pulse and starts to increase when the current returns to its baseline. This behavior is consistent with the redeposition – dissolution observed via in-situ microscopy.[15] It is only at the end of the pulse, when the redeposition rate decreases, that the Cu-dmphen complex is liberated from the dissolution-redeposition cycle and can be transported by the flowing electrolyte and detected by ICP-MS. The intensity of the signal reaches its maximum value around 200 s after the most negative pulse at $-1.2V_{RHE}$.

Detection of intermediates by optical spectroscopy

While on-line ICP-MS is a powerful method to study bulk metal dissolution, the electrochemical flow cell for ICP-MS operates in conditions which are different than those of the H-cell used to evaluate catalyst performance during CO_2RR. The experimental setup allows only for short cathodic pulses to prevent gas bubble nucleation, as gas bubbles impede reliable measurements. Furthermore, the chemical nature of the dissolved species cannot be determined by ICP-MS.

The detection of metal ions with specific chelating agents via optical spectroscopy is a routine technique in biology, where spectroscopy enables for example intracellular detection of low concentrations of free Cu ion pools.[39–41] The coordination of Cu ions by dmphen ligands generates a distinct optical response, which provides information of the oxidation state of the dissolved Cu species and offers a detection principle alternative to ICP-MS.[35,42] With this in mind, a variant of the classical H-cell typically used in CO_2RR catalyst research was designed with reduced electrolyte volume (Fig 3a).[43] This cell allows quantitative measurements of Cu

ion concentrations upon coordination with dmphen (Supplementary Note S3.1 and Fig S3.1). The static mode of operation enables the accumulation and the optical detection of the phenanthroline-bound Cu intermediate in the catholyte, thus overcoming some of the limitations previously described.

Both Cu^{+} and Cu^{2+} ions are readily coordinated by dmphen, producing $[Cu(dmphen)_2]^{+}$ or $[Cu(dmphen)_2]^{2+}$.[34,35] The formation of these complexes can be observed and quantified as only $[Cu(dmphen)_2]^{+}$ exhibits a unique absorption at 450 nm (Fig 3b). [34,35] The signal from $[Cu(dmphen)_2]^{+}$ is clearly detected at OCP (Fig 3c). The copper ion concentration calculated from the $[Cu(dmphen)_2]^{+}$ absorption intensity and that calculated from ex-situ ICP-MS data acquired under static conditions indicate that most of the copper dissolving at OCP is in the form of Cu^{+} species (Fig. 3d). Similar results were obtained for Cu foil (Supplementary Fig. S3.2). This finding indicates that the Cu dissolution at OCP occurs via Cu^{+} species.

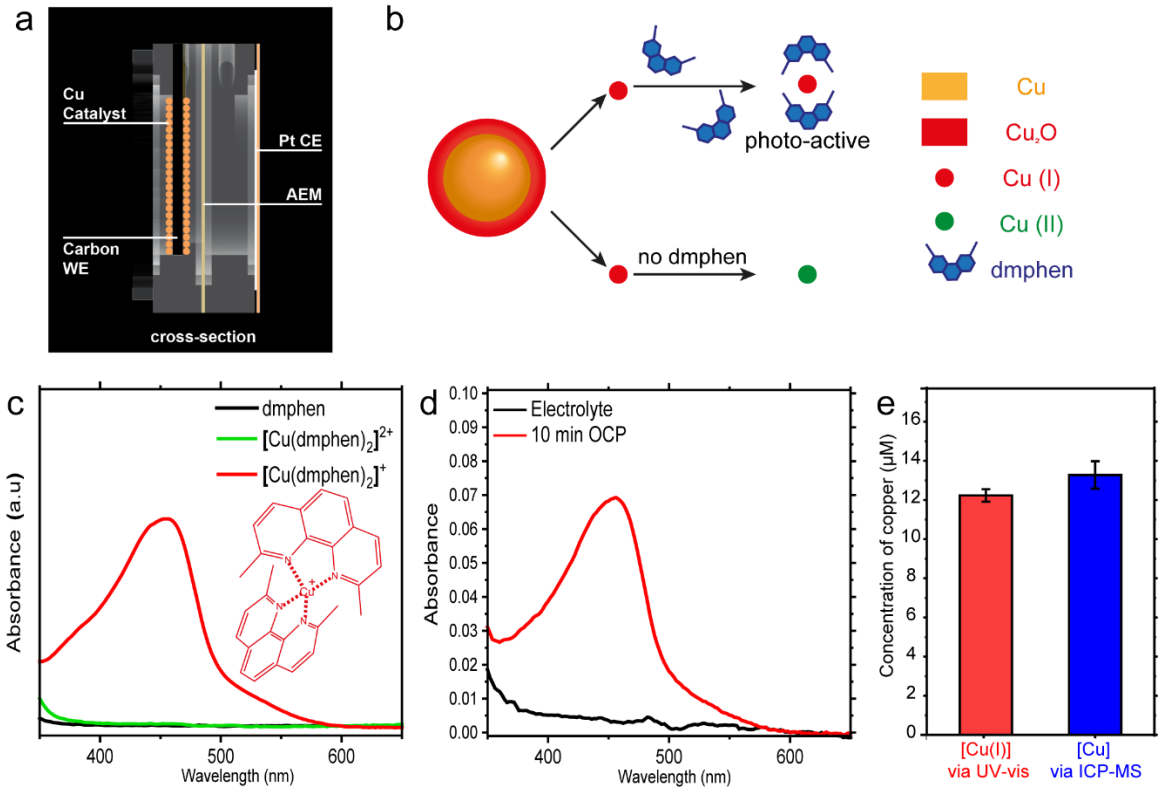

Fig. 3: Detection of Cu species via UV-Vis spectroscopy. (a) Sketch of the cell. The glassy carbon working electrode (WE) covered with the copper spheres is immersed in 1mL of 0.1M $KHCO_3$ + 0.1mM dmphen electrolyte. The potential is measured with an Ag/AgCl reference

electrode (RE). The anolyte with a Pt counter electrode (CE) is separated by an anion exchange membrane (AEM). (b) Schematic representation of the working principle of the optical measurement with dmphen as a chelating ligand. (c) UV-Vis absorption spectra of the dmphen, Cu(I) and Cu(II) complexes. (d) Representative UV-Vis spectra of the electrolyte before and after 10 min at OCP. (e) Cu concentration quantified from the same UV-Vis data (Supplementary Fig. S3.1) and ex-situ ICP-MS.

However, the $[Cu(dmphen)_2]^+$ UV-Vis signal was below the detection limit upon application of the cathodic potential during CO_2RR (Supplementary Fig. S3.3), which suggests that the kinetics of redeposition of the Cu transient species are faster than the minute scale accessible via the optical detection method. At the same time, the online ICP-MS data indicate that dmphen enables the detection of dissolved copper at OCP and under CO_2RR operating conditions in a similar manner. Thus, we speculate that Cu^+ intermediate species are equally responsible for the Cu dissolution under CO_2RR.

Control experiments and calculations allow us to confidently exclude any major interference of the dmphen ligands with the formation of the primary dissolved Cu intermediates and with the catalysis (Supplementary Notes S3.2, S3.3, S3.4 and S4.1, Supplementary Fig S3.4-3.7 and S4.7)

Computational model

In previous studies, the occurrence of the catalytic reaction itself, the electrolyte, and the effect of applied potential have been all recognized to play a role in the Cu reconstruction.[6–14] Strong binding of oxalates and carbonates has been suggested to poison the surface and influence Cu dissolution.[44,45] Hydride-mediated cathodic corrosion was proposed for noble metals.[46,47] Anomalous dissolution of Cu in acidic media under cathodic polarization was previously connected to the oxygen reduction reaction (ORR).[48–50] In addition to reaction intermediates, the cathodic bias itself was found to induce surface changes of Cu in the presence of H and CO adsorbates.[17]

The results discussed above expand the existing knowledge and indicate that Cu^+ intermediate species are generated during Cu reconstruction. However, to the best of our knowledge, spectroscopic tools which can probe the nature of these short-lived species in close proximity

of the electrode surface during operation do not exist yet. Thus, simulations were used to assess the thermodynamics of the adsorption, dissolution, and redeposition processes for CO_2RR intermediates on few representative Cu facets under the cathodic potential.

The hypothesized mechanism for the Cu dissolution – redeposition at cathodic potentials involves first the adsorption of CO_2, then the formation of adsorbed reaction intermediates, followed by the dissolution of metal-adsorbate complexes and eventual redeposition on the catalyst surface (Fig. 5a). The DFT study was performed through the PBE functional[51] and included implicit solvation effects through the VASPsol framework[52,53], and explicit electric field effects, as reported in the Methods Section. To model the experimental system, Cu(111) (6×6), Cu(100) (6×6), and Cu(711) (1×6) were considered to assess the case of close-packed domains, open facets, and low coordination sites ($N_{Cu\text{-}Cu}$ = 7 for (711)), respectively (Fig. 5b). A low surface coverage, from 0.01 to 0.03 monolayers, was kept constant in the whole study because of the large supercells utilized to accommodate the relatively large dmphen molecule. Stronger bonds between adsorbates and Cu sites weaken the bonds between Cu-Cu surface atoms, thus favoring their mobility. [25,26] In the simulation, the actual dissolution is then determined from the energetics of formation of the metal-adsorbate complex in the electrolyte, wherein solvation energy plays also an important role.

First, DFT energies of adsorption (ΔE_{ads}) for HER, ORR, and CO_2RR intermediates were obtained at U = –1.2 V_{RHE} (Supplementary Fig. S4.1). The adsorption energies correspond to the energies associated with the formation of the adsorbates ($x\mathrm{CO_2} + y\mathrm{O_2} + z\mathrm{H^+} + z\mathrm{e^-} \rightarrow *\text{adsorbate} + k\mathrm{H_2O};\ \Delta E_{\mathrm{ads}}$). Among HER and ORR intermediates, *H, *OH, and *OOH (* = adsorbed) were considered, since $*H_2O_2$ was found to dissociate on all the three Cu facets. The screening of the CO_2RR intermediates focused on *CO, *OCHO and $*C_2O_4$ as representative examples because spectroscopic studies have corroborated the existence of these species on Cu surface during CO_2RR.[45,54,55] Finally, electrolyte species (*i.e.* $*HCO_3^-$, $*CO_3^{2-}$) were also considered. The estimated adsorption energies followed well-known linear scaling relationships.[56–58] This DFT screening indicated that *H, *OH *OOH, *CO, *OCHO, $*C_2O_4$ and $*HCO_3$ (* = adsorbed) exhibit a negative ΔE_{ads}; thus, they are expected to populate the surface at the cathodic potential where CO_2RR occurs and may trigger Cu dissolution.

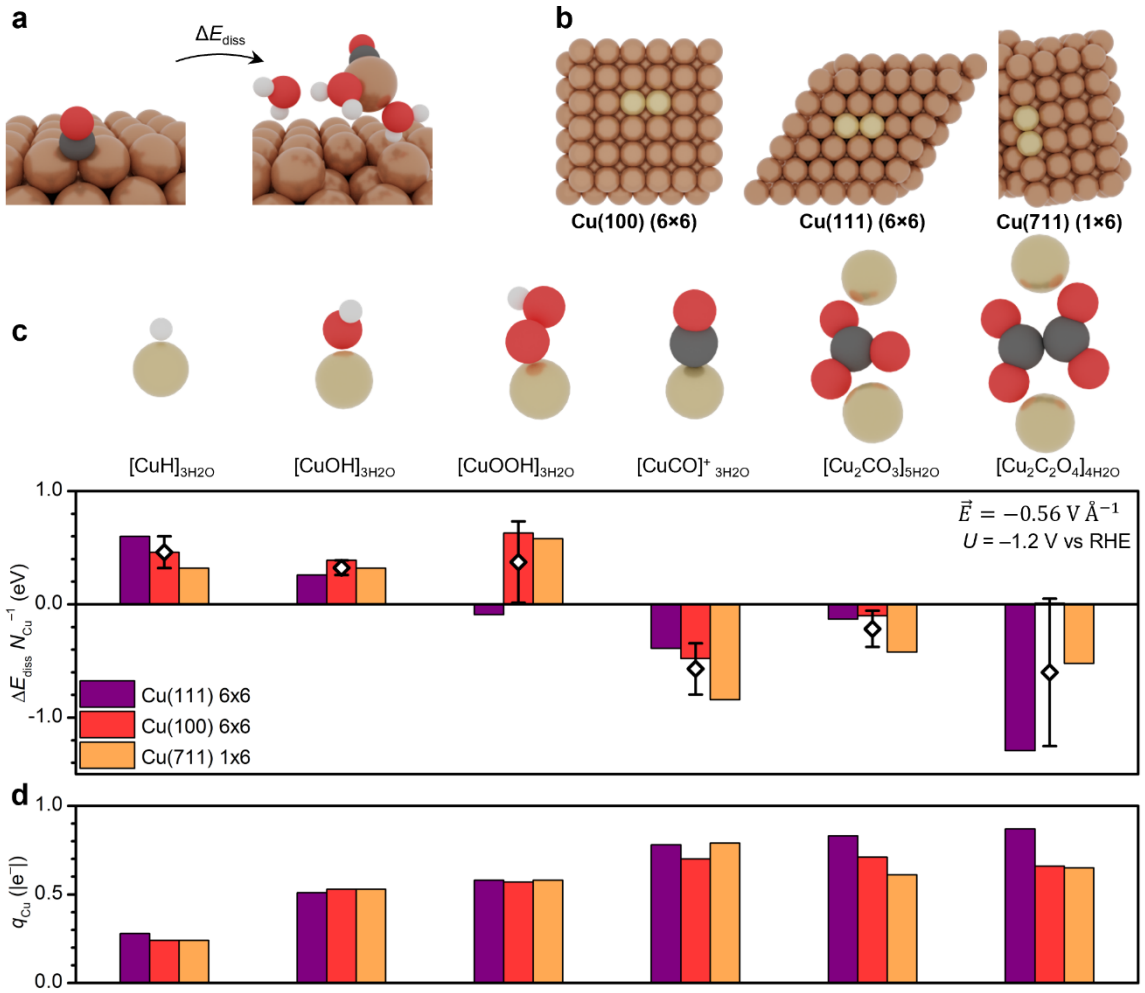

Fig. 5. Adsorbates-driven dissolution of Cu under cathodic bias. (a) Proposed mechanism for the representative case of a copper-carbonyl complex on model step surface Cu(711): first CO_2 reduces to adsorbed CO*, then the $[CuCO]^+$ complex, solvated by H_2O, dissolves close to the electrode (b) DFT models: Cu(100) 6×6, Cu(111) 6×6, and Cu(711) 1×6. Copper atom(s) that are to dissolve in solution are colored in light brown. (c) DFT energy required to form $[Cu^+L]_{aq}$ complexes in solution for low surface coverages (θ = 0.03-0.04 ML) under an applied electric field of –0.56 V Å^{-1}, equivalent to –1.2 V_{RHE} (see Methods, Supplementary Fig. S4.8, Supplementary Eq. 2, Supplementary Tables S4.4-S4.6).). From left to right, L = H, OH^-, OOH^-, CO, CO_3^{2-}, $C_2O_4^{2-}$. The subscripts indicate the number of H_2O molecules stabilizing each Cu complex. Alternative, less favorable species and/or geometries are reported in Supplementary Fig. S4.2. Data points and error bars represent averages between the three facets and half range. (d) Average Cu Bader charges for $[Cu^+L]_{aq}$ complexes.

As the second step, the stability of the corresponding metal-adsorbate complexes in the electrolyte was evaluated as dissolution energy (ΔE_{diss}), which corresponds to the energy required for their formation ($* \text{adsorbate} + n_{H_2O} \rightarrow [Cu^{+}\text{adsorbate}]_{n_{H_2O}}$; ΔE_{diss}). Since the medium is an aqueous electrolyte, it is reasonable to assume that they desorb as solvated complexes with Cu ion(s), indicated as $[Cu^{+}L]_{aq}$. To identify the adsorbates which trigger the formation of such $[Cu^{+}L]_{aq}$ complexes, the DFT energy required for a single Cu surface site to dissolve as a $[Cu^{+}L]_{aq}$ complex ($\Delta E_{diss}\ N_{Cu}^{-1}$) was estimated.

Fig. 5c reports the ΔE_{diss} at U = –1.2 V_{RHE} for some of the assessed intermediates, while Supplementary Fig. S4.2 illustrates an extended sampling. The solvated complexes were modeled with the specific number of explicit H_2O molecules that reproduces a four-coordination first solvation sphere (Supplementary Fig. 4.3), while contribution of further shells was modeled through an implicit medium.[50,51] No electrolyte cations or anions were included in the supercell at this stage. Exchange of one water ligand by one additional adsorbate was considered for two case studies (Supplementary Figure S4.2). For both intermediates, dissolution was found to be less favorable for a double ligand, which suggests that the dissolution mechanism preferentially involves single adsorbates rather than pairs. The energy differences on Cu(111), Cu(100), and Cu(711) fall within the error of the simplified solvation model utilized in this study, thus the ΔE_{diss} data are discussed as averages rather than specific values for each surfaces.

The ΔE_{diss} of $[CuH]_{3H2O}$, $[CuOH]_{3H2O}$ and $[CuOOH]_{3H2O}$ are positive, which suggest that they do not play a role in triggering the dissolution. Instead, $[CuCO]^{+}_{3H2O}$, $[Cu_2C_2O_4]_{5H2O}$ and $[Cu_2CO_3]_{4H2O}$ are all thermodynamically favored, with the formation of copper-carbonyls and copper-oxalates being the most exothermic. Furthermore, since $*CO_3$ adsorption is slightly endothermic (Supplementary Fig.4.1), this intermediate is unlikely to reach coverages high enough to enable dissolution. The same trend among the complexes persists at less negative potentials (Supplementary Fig. S4.4 and Supplementary Tables S4.1 and S4.2) and at higher surface coverages of the intermediates (Supplementary Fig. S4.5). The only exception is $[CuOH]_{3H2O}$ whose formation as a soluble species becomes more favorable at higher coverages. However, since their adsorption energy remains positive, their contribution to Cu dissolution is most likely negligible. Higher negative potentials increase the ΔE_{diss} of the $[CuCO]^{+}_{3H2O}$ (Supplementary Fig. 4.6) Furthermore, *CO binds more strongly than $*C_2O_4$ and $*CO_3$ at –1.2 V_{RHE} (Supplementary Fig. S4.1), which suggest a higher surface coverage of *CO species

under reaction conditions. Altogether, these results point at *CO to be the main intermediate species driving Cu dissolution. All the Cu-*L* species account for positive Bader charges on the copper atoms, attributable to Cu^+ oxidation state (Fig. 5d, Supplementary Fig. S4.2, Supplementary Table S4.3), which agrees with the optical spectroscopy data. It was also observed that the conversion reaction from $[CuCO]^+$ to $[Cu(dmphen)_2]^+$ is exothermic (Supplementary Fig. S4.7, Supplementary Eq. 1), confirming that the intermediate Cu complexes in solution can readily react with the dmphen facilitating their indirect detection.

Discussion

A final mechanistic picture of the copper dissolution under CO_2RR conditions emerges from the experimental and theoretical observations discussed above (Fig. 6). The surface adsorption of molecules, including carbon monoxide, carbonate, and oxalate, enables the formation of Cu-adsorbate complexes, which can dissolve in solution. Among these, the formation of $[CuCO]^+$ complexes is the most favorable regardless of the Cu surface exposed. Thus, copper carbonyl complexes emerge as the main species driving the dissolution. Nevertheless, these species are short lived in the reaction environment. The $[CuCO]^+$ complex is generally unstable and dissociates to Cu^+ ion and CO(g).[59,60] This mechanism could also explain the previously observed exchange of surface bound CO with dissolved CO, which cannot be described as an adsorption/desorption equilibrium and contribute the accumulation of CO in the close proximity of the Cu catalyst surface.[61,62] Moreover, a high local CO concentration has been previously suggested to have detrimental effect on Cu catalyst stability.[12,63] Here the mechanism through which this process takes place is finally elucidated. The redeposition process then occurs via the electrochemical reduction of the released Cu^+ to metallic Cu.

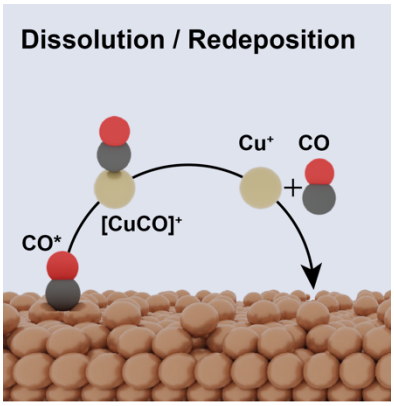

Fig.6: Schematic illustration of the copper reconstruction mechanism under CO_2RR conditions. Adsorbed CO* intermediates drive the transient dissolution followed by redeposition.

Conclusions

Cu^+ species were proposed as the major intermediates for the reconstruction via dissolution – redeposition of copper nanocatalysts which drive CO_2RR. The role of CO_2RR intermediates in this process was further assessed through DFT, including explicit electric field and solvation effects. Copper carbonyls and oxalates were suggested as the reaction-specific soluble species driving the reconstruction of Cu electrodes during operation.

Operando techniques with enough sensitivity and temporal resolution to experimentally confirm the identity of these transient soluble intermediates do not exist. This study motivates the development of these techniques and encourages research efforts on schemes which selectively target Cu^+ complexes to circumvent operational dissolution – redeposition. For example, organic layers, porous carbon materials and oxide shells might serve this purpose.[17,64-67] Alternatively, the controlled electro-(re)deposition of these intermediates to sustain catalyst selectivity and activity over extended time periods should also be considered.[68,69]

Methods

Catalyst preparation and characterization

The Cu spheres of 7nm were synthesized according to published protocols.[70,71] Two different methods were used to prepare the electrodes. Glassy carbon sheets were dip-coated in NP suspension, while the movement of the substrate was controlled via a stepper motor to provide uniform and reproducible nanoparticle films with mass loading of 12 µg on a 4 cm^2 surface as determined by elemental analysis. The usual drop-casting method, used to determine the CO_2RR performance was also used in this study. Data in the SI were collected on drop-casted samples. This technique consists in drop-casting 15 µg of copper spheres in a toluene suspension. Cu foil (99.999%) was electropolished at 2 V for 5min vs Cu foil counter electrode in 85% phosphoric acid. ECSA of prepared electrodes was estimated from a double layer capacitance in the CO_2RR cell, calculated from a CV between –0.2 $V_{Ag/AgCl}$ and –0.15 $V_{Ag/AgCl}$ from the slope of the capacitive current at –0.175 $V_{Ag/AgCl}$ plotted as a function of scan rate between 4 and 32 mV/s.

TEM analysis was done either on FEI Spirit at 120 kV or JEOL 2200 FS at 200 kV.

On-line ICP-MS

Cu dissolution was tracked with on-line ICP-MS measurements. The setup consists of an in-house designed and manufactured scanning flow cell (SFC), which outlet was coupled to the inlet of and inductively-coupled plasma mass spectrometer (Perkin Elmer NexION 350X). A double junction Ag/AgCl/3M KCl reference electrode (Metrohm) was used as the reference electrode, which was connected to the SFC via a capillary channel on the outlet side of the cell (to avoid Cl^- ion contamination). A glassy carbon rod (SIGRADUR) was applied as the counter electrode, and it was connected to the SFC on the inlet side via a T-connector. Either the freshly polished Cu foil or the spherical Cu NPs-coated glassy carbon electrode served as the working electrode. The NP-coated electrodes were identical to the ones used in the other experiments. The working electrode was placed on an XYZ stage (Physik Instrumente M-403). Electrolyte used is 0.05 M $KHCO_3$ that was saturated either with CO_2 and Ar. An experimental limit of the system where salt concentration above 0.05 M does not allow ions detection imposed the choice of this concentration over 0.1 M $KHCO_3$. The electrolyte flow (average flow rate was 3.5 µl s^{-1}) was controlled by the peristaltic pump of the ICP-MS (M2, Elemental Scientific). All electrochemical measurements were performed on a Gamry Reference 600 potentiostat.

Contact with the electrolyte was established applying –0.28 mA cm^{-2}. After a 600s hold at this current density, four current pulses were applied with gradually decreasing current densities of –0.55 (duration of the hold was 20 s), –1.1 (35s), –2.2 (45s) and –2.95 mA cm^{-2} (55 s). The current density was set back to its baseline value and held there for 120 s after each pulse, except for the last, most negative one, when the current density was left at –0.28 mA cm^{-2} for an additional 600 s. Galvanostatic electrochemical protocol was chosen to allow a better control over bubble formation under CO_2RR conditions resulting in more reliable cell operation. For further information about the optimization of measurement protocols see Section 2 in the SI. A custom-developed LabView software was used to control all instruments including the stages, potentiostat, peristaltic pump, and gas control box. ICP-MS was calibrated daily by a four-point calibration slope prepared from fresh standard solutions (Cu and Co, Merck Centripur).[61] Co served as the internal standard. The internal standard stream was merged with the sample electrolyte stream via a Y-connector before the nebulizer of the ICP-MS.

Detection of Cu ions via UV-Vis spectroscopy

An H-Cell built in-house was constructed to mimic the typical cells used in CO_2RR catalyst research. The cell geometry defines a 1 mL working electrode compartment with both faces of the electrode being exposed to the electrolyte. 2,9-dimethyl-1,10-phenanthroline (0.1 mM) was added to the 0.1M $KHCO_3$ electrolyte and sonicated in a bath sonicator until completely dissolved. Note that the unbound dimethyl-phenanthroline ligands are always in large excess to the generated Cu ions. Electrolyte was pre-saturated with CO_2, which was then continuously bubbled through the electrolyte during the experiment. Anolyte and catholyte chambers were separated with anion exchange membrane to prevent redeposition of Pt and diffusion of oxygen back to the working electrode. Working electrode (WE) was a glassy carbon sheet with 1.5 cm^2 geometric area. Counter electrode was Pt wire (99.99 %) and the used reference electrode was a leak-free Ag/AgCl LF^{-1} from Innovative Instruments Ltd. Bio-Logic SP200 potentiostat was used to bias the electrochemical cell. The potential was converted to RHE scale using Equation 1.

$$E_{RHE}\ (V) = 0.205 + E_{Ag/AgCl} + 0.059*pH \qquad \text{Equation 1}$$

To collect absorbance spectra, Perkin Elmer Lambda 950 Spectrophotometer equipped with deuterium and tungsten halide light sources and a photomultiplier tube with Peltier-controlled

PbS detector was used. Absorption of electrolyte solutions is measured between 250 and 650 nm in a 0.5mL quartz cuvette.,

The standards for the Cu^{2+} complex were prepared by dissolving 0.05 mM concentration of $CuSO_4$ in electrolyte containing 0.1 mM of dmphen. The Cu^{+} complex is first synthesized following previous literature protocols.[33] Copper(I) chloride (52.5 mg, 530 µmol) and (dmphen (221 mg, 1.06 mmol) are stirred in anhydrous ethanol (15 mL) under N_2 atmosphere for 2h. The ethanol is evaporated on a nitrogen Schlenk line to prevent reoxidation of Cu^{+} ions and a brick red solid is obtained. The solid is first diluted to 1mM in ethanol and further dilutions in water for concentrations in the range 1 to 100 µM are used for the determination of the molar absorption coefficient.

All reported measurements were performed in 0.1M $KHCO_3$ (pH=8.2) upon saturation with CO_2 (pH drops to 6.5).

Ex-situ ICP-MS was performed using NexION® 350D model with a dual-channel Universal Cell. The as-prepared samples were digested in 2% nitric acid.

Computational Details

DFT simulations were applied through the Vienna Ab Initio Simulation Package (VASP), employing PBE as density functional[51] and van der Waals dispersion through the DFT-D2 method[72,73] with our reparametrized C_6 coefficients.[74] To account for solvent contribution to Cu species formation energy, we employed the VASPsol code.[52,53] Meanwhile, the explicit electric field was included through a dipole correction.[74,75] Electric field was converted to electric potential vs RHE according to Equation 2, where U_{pzc} is the potential of zero charge (vs RHE) and d is the thickness of the electrical double layer, estimated as 3 Å.[76] Since the electric potential applied experimentally (–1.2 V_{RHE}) was beyond the values achievable through DFT simulations, an extrapolation protocol was developed. According to Refs.[17,76] the DFT energy of surfaces and intermediates depends on the electric field through Equation 3. In presence of electric field, firstly the energy of an intermediate changes by an interaction term $E_{\text{int}} = \vec{p} \cdot \vec{E} - \frac{1}{2}\alpha\vec{E}^2$, which depends on its dipole moment $\vec{p}$ and polarizability α.[76] Secondly, the energy of the surface itself is affected by applied electric field through an electrostatic term $E_{\text{el}} = -\frac{1}{2}\varepsilon A d$, where $\varepsilon A d$ term indicates the electrostatic energy stored by the surface at cathodic

bias, estimated assuming the electrical double layer as a parallel plate capacitor with ε is the dielectric permittivity of the medium (electrolyte), A the electrode surface area, and d the thickness of the dielectric double layer.[76] This hypothesis is valid at the large electrolyte concentrations and large polarization in dilute media characteristic of the experimental conditions.[77] Thus, DFT energies of Cu surfaces, adsorbates, and Cu complexes were obtained for $\vec{E}$ between –0.3 and +0.3 V Å^{-1}, and the function E($\vec{E}$) fitted according to Equation 3 (Supplementary Fig. S4.4). Then, DFT values at –1.2 V vs RHE ($\vec{E}$ = –0.56 V Å^{-1}, see Equation 2) were estimated through Equation 3 according to the fitting parameters (Supplementary Tables S4.4-S4.6).

$$U = U_{\mathrm{pzc}} + \vec{E}d \qquad \text{Equation 2}$$

$$E(\vec{E}) = E_0 + E_{\mathrm{int}} + E_{\mathrm{el}} = E(\vec{E} = 0\ V\ \text{Å}^{-1}) + \vec{p}\cdot\vec{E} - \frac{1}{2}(\alpha + \varepsilon A d)\vec{E}^2 \qquad \text{Equation 3}$$

Inner electrons were represented through PAWpseudopotentials[78,79] and the monoelectronic states corresponding to valence electrons were expanded as plane waves with a kinetic energy cutoff of 450 eV. Three structural models were employed, namely Cu(100) 6×6, Cu(111) 6×6, and Cu(711) 6×6. On as-synthesized Cu nanoparticles, (111) domains are expected to be the most abundant according to Wulff theorem due to their low surface energy[80], and may evolve to (100) and defective sites, modeled as Cu(711) here, under electrochemical conditions.[6,81]All the crystalline slabs contained at least four equivalent layers, with the two outermost relaxed and the rest fixed to the bulk distances. Vacuum thickness between periodic repetitions of the slabs accounted for at least 15 Å. We sampled the Brillouin zone by a Γ-centered k-points mesh from the Monkhorst-Pack method,[82] with a reciprocal grid size smaller than 0.03 Å^{-1}. Each selected Cu-*L* complexes was set at a distance of more than 3 Å from the surface on one side of the periodic cell, thus we imposed a dipole correction to correct artifacts from the asymmetric slab model.[83] We reported all adsorption and dissolution energies using CO_2(g), H_2(g), H_2O(g), dimethyl-phenanthroline(g) and the clean surface as energy references, according to Equations 4 and 5. When needed, CO(g) energy was estimated from DFT and experimental values following the procedure described in Ref.[84]

$$x\mathrm{CO_2} + y\mathrm{O_2} + z\mathrm{H^+} + z\mathrm{e^-} \rightarrow * \text{adsorbate} + k\mathrm{H_2O};\ \Delta E_{ads} \qquad \text{Equation 4}$$

$$* \text{adsorbate} + n_{\mathrm{H_2O}} \rightarrow [\mathrm{Cu^+}\text{adsorbate}]_{n_{\mathrm{H_2O}}};\ \Delta E_{diss} \qquad \text{Equation 5}$$

Data availability

The datasets generated though DFT and analysed during the current study are available in the ioChem-BD database[85] at DOI 10.19061/iochem-bd-1-231, currently under embargo. Reviewers can access the full dataset here: https://iochem-bd.iciq.es/browse/review-collection/100/36205/23ee811de59d952e37462864. Experimental data are openly available at DOI: 10.5281/zenodo.6724739.

Acknowledgements

G. R. acknowledges the financial support of the Ecole Normale Supérieure Paris Saclay. P.P.A. thanks NCCR Catalysis (grant number 180544), a National Centre of Competence in Research funded by the Swiss National Science Foundation for financial support. F.D. and N.L. acknowledge the financial support by the Spanish Ministry of Science and Innovation (RTI2018-101394-B-I00, Severo Ochoa CEX2019-000925-S) and the Barcelona Supercomputing Center (BSC-RES) for providing generous computational resources. Besides, F.D. and N.L. thank Dr. M. A. Ortuño and Dr. S. J. Raaijman for fruitful scientific discussions. The authors thank Dr M. Newton for assistance in the operando X-Ray absorption measurements and analysis of the corresponding data reported in the supporting information. Prof. O. Wenger is acknowledged for discussion on the phenanthroline ligands. The Swiss Norwegian beamlines (SNBL at ESRF are acknowledged for provision of beamtime and its staff for invaluable support. The BM31 setup was funded by the Swiss National Science Foundation (grant 206021_189629) and the Research Council of Norway (grant 296087). Dr Natalia Gasilova is acknowledged for assistance in the *ex-situ* ICP-MS measurements.

References

1. Nitopi, S. *et al.* Progress and Perspectives of Electrochemical CO_2 Reduction on Copper in Aqueous Electrolyte. *Chem. Rev.* **119**, 7610–7672 (2019) DOI:10.1021/acs.chemrev.8b00705.

2. Huang, J. & Buonsanti, R. Colloidal Nanocrystals as Heterogeneous Catalysts for Electrochemical CO_2 Conversion. *Chem. Mater.* **31**, 13–25 (2019) DOI:10.1021/acs.chemmater.8b04155.

3. Hahn, C. *et al.* Engineering Cu surfaces for the electrocatalytic conversion of CO_2: Controlling selectivity toward oxygenates and hydrocarbons. *Proc. Natl. Acad. Sci. U. S. A.* **114**, 5918–5923 (2017) DOI:10.1073/pnas.1618935114.

4. She, Z. W. *et al.* Combining theory and experiment in electrocatalysis: Insights into materials design. *Science* 355 (2017) DOI:10.1126/science.aad4998.

5. Schouten, K. J. P., Pérez Gallent, E. & Koper, M. T. M. Structure sensitivity of the electrochemical reduction of carbon monoxide on copper single crystals. *ACS Catal.* **3**, 1292–1295 (2013) DOI:10.1021/cs4002404.

6. Kim, Y. G., Baricuatro, J. H., Javier, A., Gregoire, J. M. & Soriaga, M. P. The evolution of the polycrystalline copper surface, first to Cu(111) and then to Cu(100), at a fixed CO_2RR potential: A study by operando EC-STM. *Langmuir* **30**, 15053–15056 (2014) DOI:10.1021/la504445g.

7. Manthiram, K., Beberwyck, B. J. & Alivisatos, A. P. Enhanced electrochemical methanation of carbon dioxide with a dispersible nanoscale copper catalyst. *J. Am. Chem. Soc.* **136**, 13319–13325 (2014) DOI:10.1021/ja5065284.

8. Gunathunge, C. M. *et al.* Spectroscopic Observation of Reversible Surface Reconstruction of Copper Electrodes under CO_2 Reduction. *J. Phys. Chem. C* **121**, 12337–12344 (2017) DOI:10.1021/acs.jpcc.7b03910.

9. Kim, D., Kley, C. S., Li, Y. & Yang, P. Copper nanoparticle ensembles for selective electroreduction of CO_2 to C2–C3 products. *Proc. Natl. Acad. Sci. U. S. A.* **114**, 10560–10565 (2017) DOI:10.1073/pnas.1711493114.

10. Grosse, P. *et al.* Dynamic Changes in the Structure, Chemical State and Catalytic Selectivity of Cu Nanocubes during CO_2 Electroreduction: Size and Support Effects. *Angew. Chemie* **130**, 6300–6305 (2018) DOI:10.1002/ANGE.201802083.

11. Huang, J. *et al.* Potential-induced nanoclustering of metallic catalysts during electrochemical CO_2 reduction. *Nat. Commun.* **9**, 3117-3126 (2018) DOI:10.1038/s41467-018-05544-3.

12. Osowiecki, W. T. *et al.* Factors and Dynamics of Cu Nanocrystal Reconstruction under CO_2 Reduction. *ACS Appl. Energy Mater.* **2**, 7744–7749 (2019) DOI:10.1021/acsaem.9b01714.

13. Jung, H. *et al.* Electrochemical Fragmentation of Cu_2O Nanoparticles Enhancing Selective C-C Coupling from CO_2 Reduction Reaction. *J. Am. Chem. Soc.* **141**, 4624–4633 (2019) DOI:10.1021/jacs.8b11237.

14. Grosse, P. *et al.* Dynamic transformation of cubic copper catalysts during CO_2

electroreduction and its impact on catalytic selectivity. *Nat. Commun.* **12**, (2021) DOI:10.1038/s41467-021-26743-5.

15. Vavra, J., Shen, T. H., Stoian, D., Tileli, V. & Buonsanti, R. Real-time Monitoring Reveals Dissolution/Redeposition Mechanism in Copper Nanocatalysts during the Initial Stages of the CO_2 Reduction Reaction. *Angew. Chemie - Int. Ed.* **60**, 1347–1354 (2021) DOI:10.1002/anie.202011137.

16. Hong Lee, S. *et al.* Oxidation State and Surface Reconstruction of Cu under CO_2 Reduction Conditions from In Situ X-ray Characterization. *J. Am. Chem. Soc* **143**, 2022 (2021) DOI:10.1021/jacs.0c10017.

17. Phan, T. H. *et al.* Emergence of Potential-Controlled Cu-Nanocuboids and Graphene-Covered Cu-Nanocuboids under Operando CO_2 Electroreduction. *Nano Lett.* **21**, 2059–2065 (2021) DOI:10.1021/acs.nanolett.0c04703.

18. Speck, F. D. & Cherevko, S. Electrochemical copper dissolution: A benchmark for stable CO_2 reduction on copper electrocatalysts. *Electrochem. commun.* **115**, (2020) DOI:10.1016/j.elecom.2020.106739.

19. Simon, G. H., Kley, C. S. & Roldan Cuenya, B. Potential-Dependent Morphology of Copper Catalysts During CO_2 Electroreduction Revealed by In Situ Atomic Force Microscopy. *Angew. Chemie - Int. Ed.* **60**, 2561–2568 (2021) DOI:10.1002/anie.202010449.

20. Raaijman, S. J., Arulmozhi, N. & Koper, M. T. M. Morphological Stability of Copper Surfaces under Reducing Conditions. *ACS Appl. Mater. Interfaces* **13**, 48730–48744 (2021) DOI:10.1021/acsami.1c13989.

21. Hochfilzer, D. *et al.* The Importance of Potential Control for Accurate Studies of Electrochemical CO Reduction. *ACS Energy Lett.* **6**, 1879–1885 (2021) DOI:10.1021/acsenergylett.1c00496.

22. Li, Y. *et al.* Structure-Sensitive CO_2 Electroreduction to Hydrocarbons on Ultrathin 5-fold Twinned Copper Nanowires. *Nano Lett.* **17**, 1312–1317 (2017) DOI:10.1021/acs.nanolett.6b05287.

23. Popovic, S., Bele, M. & Hodnik, N. Reconstruction of Copper Nanoparticles at Electrochemical CO_2 Reduction Reaction Conditions Occurs via Two-step Dissolution/Redeposition Mechanism. *ChemElectroChem* **8**, 2634–2639 (2021) DOI:10.1002/celc.202100387.

24. McCafferty, E. Thermodynamics of Corrosion: Pourbaix Diagrams. In: Introduction to Corrosion Science. *Springer, New York, NY* 328 (2010).

25. Eren, B., Weatherup, R. S., Liakakos, N., Somorjai, G. A. & Salmeron, M. Dissociative Carbon Dioxide Adsorption and Morphological Changes on Cu(100) and Cu(111) at Ambient Pressures. *J. Am. Chem. Soc.* **138**, 8207–8211 (2016) DOI:10.1021/jacs.6b04039.

26. Eren, B. *et al.* Activation of Cu(111) surface by decomposition into nanoclusters driven by CO adsorption. *Science* **351**, 475–478 (2016) DOI:10.1126/science.aad8868.

27. Xu, L. *et al.* Formation of active sites on transition metals through reaction-driven migration of surface atoms. *Science* **380**, 70-76 (2023) DOI: 10.1126/science.add0089.

28. Amirbeigiarab, R. Tian, J., Herzog, A. *et al.* Atomic-scale surface restructuring of copper electrodes under CO2 electroreduction conditions. *Nat. Catal.* (2023) DOI: 10.1038/s41929-023-01009-z.

29. Li, Y. *et al.* Electrochemically scrambled nanocrystals are catalytically active for CO_2-to-multicarbons. *Proc. Natl. Acad. Sci. U. S. A.* **117**, 9194–9201 (2020) DOI:10.1073/pnas.1918602117.

30. Yang, Y. et al. Operando studies reveal active Cu nanograins for CO_2 electroreduction. *Nature* **614**, 262-269 (2023).

31. Kasian, O., Geiger, S., Mayrhofer, K. J. J. & Cherevko, S. Electrochemical On-line ICP-MS in Electrocatalysis Research. *Chemical Record* vol. 19 2130–2142 (2019) DOI:10.1002/tcr.201800162.

32. Cherevko, S., Kulyk, N. & Mayrhofer, K. J. J. Durability of platinum-based fuel cell electrocatalysts: Dissolution of bulk and nanoscale platinum. *Nano Energy* **29**, 275–298 (2016) DOI:10.1016/j.nanoen.2016.03.005.

33. Cherevko, S. Electrochemical dissolution of noble metals native oxides. *J. Electroanal. Chem.* **787**, 11–13 (2017) DOI:10.1016/j.jelechem.2017.01.029.

34. Pallenberg, A. J., Koenig, K. S. & Barnhart, D. M. Synthesis and Characterization of Some Copper(I) Phenanthroline Complexes. *Inorg. Chem* **34**, 2833–2840 (1995) DOI:10.1021/ic00115a009.

35. Armaroli, N. Photoactive mono-and polynuclear Cu(I)-phenanthrolines. A viable alternative to Ru(II)-polypyridines? *Chem. Soc. Rev.* 113-124 (2001) doi:10.1039/b000703j DOI:10.1039/b000703j.

36. Wang, J. *et al.* A Water-Soluble Cu Complex as Molecular Catalyst for Electrocatalytic CO_2 Reduction on Graphene-Based Electrodes. *Adv. Energy Mater.* **9**, 1803151 (2019) DOI:10.1002/aenm.201803151.

37. Ruthkosky, M., Castellano, F. N. & Meyer, G. J. Photodriven Electron and Energy Transfer from Copper Phenanthroline Excited States. *Inorg. Chem.* **35**, 6406–6412 (1996) DOI:10.1021/ic960503z.

38. Soo, J. L., Doo, R. B., Won, S. H., Shim, S. L. & Jong, H. J. Different morphological organic-inorganic hybrid nanomaterials as fluorescent chemosensors and adsorbents for CuII ions. *Eur. J. Inorg. Chem.* 1559–1564 (2008) DOI:10.1002/ejic.200701073.

39. Fahrni, C. J. Synthetic fluorescent probes for monovalent copper. *Curr. Opin. Chem. Biol.* **17**, 656–662 (2013) DOI:10.1016/J.CBPA.2013.05.019.

40. Price, K. A. *et al.* The challenges of using a copper fluorescent sensor (CS1) to track intracellular distributions of copper in neuronal and glial cells. *Chem. Sci.* **3**, 2748–2759 (2012) DOI:10.1039/C2SC20397A.

41. Taki, M., Iyoshi, S., Ojida, A., Hamachi, I. & Yamamoto, Y. Development of highly sensitive fluorescent probes for detection of intracellular copper(I) in living systems. *J. Am. Chem. Soc.* **132**, 5938–5939 (2010) DOI:10.1021/ja100714p.

42. Smith, G. F., McCurdy, W. H. Jr. 2,9-Dimethyl-1,10-phenanthroline. Analytical Chemistry **24**, 371-373 (1952) DOI:10.1021/ac60062a029

43. Garg, S. *et al.* Advances and challenges in electrochemical CO_2 reduction processes: an engineering and design perspective looking beyond new catalyst materials. *J. Mater. Chem. A* **8**, 1511–1544 (2020) DOI:10.1039/C9TA13298H.

44. Velasco-Vélez, J. J. *et al.* The Role of the Copper Oxidation State in the Electrocatalytic Reduction of CO_2 into Valuable Hydrocarbons. *ACS Sustain. Chem. Eng.* **7**, 1485–1492 (2019) DOI:10.1021/acssuschemeng.8b05106.

45. Dattila, F., Garcia-Muelas, R. & López, N. Active and Selective Ensembles in Oxide-Derived Copper Catalysts for CO_2 Reduction. *ACS Energy Lett.* **5**, 3176–3184 (2020) DOI:10.1021/acsenergylett.0c01777.

46. McCrum, I. T., Bondue, C. J. & Koper, M. T. M. Hydrogen-Induced Step-Edge Roughening of Platinum Electrode Surfaces. *J. Phys. Chem. Lett.* **10**, 6842–6849 (2019) DOI:10.1021/acs.jpclett.9b02544.

47. Hersbach, T. J. P. & Koper, M. T. M. Cathodic corrosion: 21st century insights into a 19th century phenomenon. *Current Opinion in Electrochemistry* vol. 26 100653 (2021) DOI:10.1016/j.coelec.2020.100653.

48. Kreizer, I. V., Tutukina, N. M., Zartsyn, I. D. & Marshakov, I. K. The dissolution of a copper cathode in acidic chloride solutions. *Prot. Met.* **38**, 226–232 (2002) DOI:10.1023/A:1015609103529.

49. Kreizer, I. V., Marshakov, I. K., Tutukina, N. M. & Zartsyn, I. D. Partial reactions of copper dissolution under cathodic polarization in acidic media. *Prot. Met.* **40**, 23–25 (2004) DOI:10.1023/B:PROM.0000013107.65745.b0.

50. Kreizer, V., Marshakov, I. K., Tutukina, N. M. & Zartsyn, I. D. The Effect of Oxygen on Copper Dissolution during Cathodic Polarization. *Prot. Met.* **39**, 30–33 (2003) DOI:10.1023/A:1021935023079.

51. Perdew, J. P., Burke, K. & Ernzerhof, M. Generalized Gradient Approximation Made Simple. *Phys. Rev. Lett.* **77**, 3865 (1996) DOI:10.1103/PhysRevLett.77.3865.

52. Fishman, M., Zhuang, H. L., Mathew, K., Dirschka, W. & Hennig, R. G. Accuracy of exchange-correlation functionals and effect of solvation on the surface energy of copper. *Phys. Rev. B - Condens. Matter Mater. Phys.* **87**, 245402 (2013) DOI:10.1103/PhysRevB.87.245402.

53. Mathew, K., Sundararaman, R., Letchworth-Weaver, K., Arias, T. A. & Hennig, R. G. Implicit solvation model for density-functional study of nanocrystal surfaces and reaction pathways. *J. Chem. Phys.* **140**, 084106 (2014) DOI:10.1063/1.4865107.

54. Moradzaman, M. & Mul, G. In Situ Raman Study of Potential-Dependent Surface Adsorbed Carbonate, CO, OH, and C Species on Cu Electrodes During Electrochemical Reduction of CO_2. *ChemElectroChem* **8**, 1478–1485 (2021) DOI:10.1002/celc.202001598.

55. Kim, Y. *et al.* Time-resolved observation of C-C coupling intermediates on Cu electrodes for selective electrochemical CO_2 reduction. *Energy Environ. Sci.* **13**, 4301–4311 (2020) DOI:10.1039/d0ee01690j.

56. Calle-Vallejo, F., Martínez, J. I., García-Lastra, J. M., Sautet, P. & Loffreda, D. Fast prediction of adsorption properties for platinum nanocatalysts with generalized

coordination numbers. *Angew. Chemie - Int. Ed.* **53**, 8316–8319 (2014) DOI:10.1002/anie.201402958.

57. Calle-Vallejo, F. *et al.* Finding optimal surface sites on heterogeneous catalysts by counting nearest neighbors. *Science.* **350**, 185–189 (2015) DOI:10.1126/science.aab3501.

58. Calle-Vallejo, F., Loffreda, D., Koper, M. T. M. & Sautet, P. Introducing structural sensitivity into adsorption-energy scaling relations by means of coordination numbers. *Nat. Chem.* **7**, 403–410 (2015) DOI:10.1038/nchem.2226.

59. Pasquali, M., Floriani, C. & Gaetani-Manfredotti, A. Carbon Monoxide Absorption by Copper(I) Halides in Organic Solvents: Isolation and Structure of μ-Halogeno-dicopper(I) Carbonyl Complexes. *Inorg. Chem.* **20**, 3382–3388 (1981) DOI:10.1021/ic50224a046.

60. Pike, R. D. Structure and bonding in copper(I) carbonyl and cyanide complexes. *Organometallics* vol. 31 7647–7660 (2012) DOI:10.1021/om3004459.

61. Wuttig, A. *et al.* Tracking a common surface-bound intermediate during CO_2-to-fuels catalysis. *ACS Cent. Sci.* **2**, 522–528 (2016) DOI:10.1021/acscentsci.6b00155.

62. Clark, E. L. & Bell, A. T. Direct Observation of the Local Reaction Environment during the Electrochemical Reduction of CO_2. *J. Am. Chem. Soc.* **140**, 7012–7020 (2018) DOI:10.1021/jacs.8b04058.

63. Wilde, P.; O'Mara, P. B.; Junqueira, J. R. C.; Tarnev, T.; Benedetti, T. M.; Andronescu, C.; Chen, Y.-T.; Tilley, R. D.; Schuhmann, W.; Gooding, J. J. Is Cu Instability during the CO_2 Reduction Reaction Governed by the Applied Potential or the Local CO Concentration? *Chem. Sci.* **2021**, *12* (11), 4028–4033. https://doi.org/10.1039/D0SC05990K.

64. Li, Y. *et al.* Structure-Sensitive CO_2 Electroreduction to Hydrocarbons on Ultrathin 5-fold Twinned Copper Nanowires. *Nano Lett.* **17**, 1312–1317 (2017) DOI:10.1021/acs.nanolett.6b05287.

65. Zhang, X. Y. *et al.* Selective methane electrosynthesis enabled by a hydrophobic carbon coated copper core–shell architecture. *Energy Environ. Sci.* **15**, 234–243 (2022) DOI:10.1039/D1EE01493E.

66. Paolucci, C. *et al.* Dynamic multinuclear sites formed by mobilized copper ions in NO_x selective catalytic reduction. *Science.* **357**, 898–903 (2017) DOI:10.1126/science.aan5630.

67. Zhang, L. *et al.* A Polymer Solution To Prevent Nanoclustering and Improve the Selectivity of Metal Nanoparticles for Electrocatalytic CO_2 Reduction. *Angew. Chemie - Int. Ed.* **58**, 15834–15840 (2019) DOI:10.1002/anie.201909069.

68. Timoshenko, J. *et al.* Steering the structure and selectivity of CO_2 electroreduction catalysts by potential pulses. *Nat. Catal.* **5**, 259–267 (2022) DOI:10.1038/s41929-022-00760-z.

69. Kim, C., Weng, L. C. & Bell, A. T. Impact of Pulsed Electrochemical Reduction of CO_2 on the Formation of C2+ Products over Cu. *ACS Catal.* **10**, 12403–12413 (2020) DOI:10.1021/acscatal.0c02915.

70. Hung, L.-I., Tsung, C.-K., Huang, W. & Yang, P. Room-Temperature Formation of Hollow Cu_2O Nanoparticles. *Adv. Mater.* **22**, 1910–1914 (2010) DOI:10.1002/adma.200903947.

71. Loiudice, A. *et al.* Tailoring Copper Nanocrystals towards C2 Products in Electrochemical CO_2 Reduction. *Angew. Chemie - Int. Ed.* **55**, 5789–5792 (2016) DOI:10.1002/anie.201601582.

72. Grimme, S. Semiempirical GGA-type density functional constructed with a long-range dispersion correction. *J. Comput. Chem.* **27**, 1787–1799 (2006) DOI:10.1002/jcc.20495.

73. Bučko, T., Hafner, J., Lebègue, S. & Ángyán, J. G. Improved description of the structure of molecular and layered crystals: Ab initio DFT calculations with van der Waals corrections. *J. Phys. Chem. A* **114**, 11814–11824 (2010) DOI:10.1021/jp106469x.

74. Almora-Barrios, N., Carchini, G., Błoński, P. & López, N. Costless derivation of dispersion coefficients for metal surfaces. *J. Chem. Theory Comput.* **10**, 5002–5009 (2014) DOI:10.1021/ct5006467.

75. Feibelman, P. J. Surface-diffusion mechanism versus electric field: Pt/Pt(001). *Phys. Rev. B* **64**, 125403 (2001) DOI:10.1103/PhysRevB.64.125403.

76. Chen, L. D., Urushihara, M., Chan, K. & Nørskov, J. K. Electric Field Effects in Electrochemical CO_2 Reduction. *ACS Catal.* **6**, 7133–7139 (2016) DOI:10.1021/acscatal.6b02299.

77. Bard, A. L. & Faulkner, L. R. *Electrochemical Methods: Fundamentals and Applications,*. (Wiley).

78. Blöchl, P. E. Projector augmented-wave method. *Phys. Rev. B* **50**, 17953 (1994) DOI:10.1103/PhysRevB.50.17953.

79. Kresse, G. & Joubert, D. From ultrasoft pseudopotentials to the projector augmented-wave method. *Phys. Rev. B* **59**, 1758 (1999) DOI:10.1103/PhysRevB.59.1758.

80. Wulff, G. XXV. Zur Frage der Geschwindigkeit des Wachsthums und der Auflösung der Krystallflächen. *Zeitschrift für Krist. - Cryst. Mater.* **34**, 449–530 (1901) DOI:10.1524/ZKRI.1901.34.1.449.

81. Kim, Y. G. *et al.* Surface reconstruction of pure-Cu single-crystal electrodes under CO-reduction potentials in alkaline solutions: A study by seriatim ECSTM-DEMS. *J. Electroanal. Chem.* **780**, 290–295 (2016) DOI:10.1016/j.jelechem.2016.09.029.

82. Monkhorst, H. J. & Pack, J. D. Special points for Brillouin-zone integrations. *Phys. Rev. B* **13**, 5188 (1976) DOI:10.1103/PhysRevB.13.5188.

83. Makov, G. & Payne, M. C. Periodic boundary conditions in *ab initio* calculations. *Phys. Rev. B* **51**, 4014 (1995) DOI:10.1103/PhysRevB.51.4014.

84. Granda-Marulanda, L. P. *et al.* A Semiempirical Method to Detect and Correct DFT-Based Gas-Phase Errors and Its Application in Electrocatalysis. *ACS Catal.* **10**, 6900–6907 (2020) DOI:10.1021/acscatal.0c01075.

85. Álvarez-Moreno, M. *et al.* Managing the computational chemistry big data problem: The ioChem-BD platform. *J. Chem. Inf. Model.* **55**, 95–103 (2015) DOI:10.1021/ci500593j.